Understanding the Influence of $Li_7La_3Zr_2O_{12}$ Nanofibers on Critical Current Density and Coulombic Efficiency in Composite Polymer Electrolytes

Michael J. Counihan[1], Devon J. Powers[2], Pallab Barai[2], Shiyu Hu[2], Teodora Zagorac[4], Yundong Zhou[5], Jungkuk Lee[2], Justin G. Connell[3], Kanchan S. Chavan[6], Ian S. Gilmore[5], Luke Hanley[4], Venkat Srinivasan[6], Yuepeng Zhang[2]*, Sanja Tepavcevic[1]*

[1]Materials Science Division, Argonne National Laboratory, Lemont, IL 60439, United States
[2]Applied Materials Division, Argonne National Laboratory, Lemont, IL 60439, United States
[3]Joint Center for Energy Storage Research, Argonne National Laboratory, Lemont, IL 60439, United States
[4]University of Illinois Chicago, Chemistry (MC 111), Chicago, IL 60607, United States
[5]National Physical Laboratory, NiCE-MSI, Teddington, Middlesex, United Kingdom
[6]Chemical Sciences and Engineering Division, Argonne National Laboratory, Lemont, IL 60439, United States

*yuepeng@anl.gov
*sanja@anl.gov

ORCID IDs:

MJC: 0000-0003-4535-573X
DJP: 0000-0001-6850-8458
PB: 0000-0003-2217-6392
SH: 0000-0003-1995-2848
TZ: 0000-0001-7467-8736
YZho: 0000-0001-9222-5722
JL: 0000-0003-2049-3749
JGC: 0000-0002-2979-2131
KSC: 0000-0003-4540-495X
ISG: 0000-0002-0981-2318
LH: 0000-0001-7856-1869
VS: 0000-0002-1248-5952
YZha: 0000-0002-6520-2880
ST: 0000-0003-0151-8832

Abstract

Composite polymer electrolytes (CPEs) are attractive materials for solid-state lithium metal batteries, owing to their high ionic conductivity from ceramic ionic conductors and flexibility from polymer components. As with all lithium metal batteries, however, CPEs face the challenge of dendrite formation and propagation. Not only does this lower the critical current density (CCD) before cell shorting, but the uncontrolled growth of lithium deposits may limit Coulombic efficiency (CE) by creating dead lithium. Here, we present a fundamental study on how the ceramic components of CPEs influence these characteristics. CPE membranes based on poly(ethylene oxide) and lithium bis(trifluoromethanesulfonyl)imide (PEO-LiTFSI) with $Li_7La_3Zr_2O_{12}$ (LLZO) nanofibers were fabricated with industrially relevant roll-to-roll manufacturing techniques. Galvanostatic cycling with lithium symmetric cells shows that the CCD can be tripled by including 50 wt% LLZO, but half cell cycling reveals this comes at the cost of CE. Varying the LLZO loading shows that even a small amount of LLZO drastically lowers the CE, from 88% at 0 wt% LLZO to 77% at just 2 wt% LLZO. Mesoscale modelling reveals that the increase in CCD cannot be explained by an increase in the macroscopic or microscopic stiffness of the electrolyte; only the microstructure of the LLZO nanofibers in the PEO-LiTFSI matrix slows dendrite growth by presenting physical barriers that the dendrites must push or grow around. This tortuous lithium growth mechanism around the LLZO is corroborated with mass spectrometry imaging. This work highlights important elements to consider in the design of CPEs for high-efficiency lithium metal batteries.

Introduction

The need for high energy density batteries in electric vehicles has created a push for lithium metal anodes and solid-state electrolytes that are stable against lithium.[1,2] Composite polymer electrolytes (CPEs) with Li^+-conducting ceramic fillers in a polymer matrix have attracted interest due to the potential for high room temperature conductivity (≥0.1 mS/cm) while maintaining mechanical flexibility and strength.[3] Cubic $Li_7La_3Zr_2O_{12}$ (LLZO) is widely used as a ceramic filler, having inherently high conductivity around 1 mS/cm at 25 °C while being relatively safe and stable in air.[4,5] Several studies have utilized LLZO nanoparticles[6,7] or more recently nanofibers/nanowires[8,9,10] and other fibrous microstructures[11,12] in polymers with lithium salts. Overall bulk ionic conductivity can be increased with small amounts of LLZO (typically <10-15 wt%) through polymer plasticizing and other effects at the LLZO-polymer interface. However, higher LLZO loadings tend to sabotage conductivity[13,14,15] unless a pre-formed nanofiber network is constructed and infiltrated with polymer after the fact,[16,17] a method which may limit processing at scale.[3]

While most CPE studies focus on increasing bulk ionic conductivity by modifying the chemistry or loading of the ceramic component, relatively little attention is paid to how this fundamentally increases the charging rates or influences battery efficiency long-term. Critical current density (CCD) is one of the prototypical measures of success for CPEs: the greater the CCD, the faster the battery can charge. However, this alone does not mean the electrolyte will perform well at the practical cell level. An understudied metric in the solid-state battery field is Coulombic efficiency (CE), the amount of charge accessible in the discharge step following charging. Most CE reports focus on how the cathode efficiency behaves with a thick lithium anode.[18-20] However, the emergence of anode-free and low-excess lithium cell designs for high energy density applications makes Coulombic efficiency at the anode a very important metric for long-life batteries.[21-23] The role of all relevant chemistries in the CPEs – polymer, salt, and ceramic – in determining CCD and CE needs to be addressed if CPEs are to remain relevant in solid-state lithium battery development.

Here, we present a systematic study of LLZO nanofiber influence on critical current density, Coulombic efficiency, and lithium dendrite growth mechanisms. CPEs based on poly(ethylene oxide) (PEO) and lithium bis(trifluoromethanesulfonyl)imide (LiTFSI) with 0-74 wt% LLZO nanofibers were fabricated with scalable roll-to-roll electrospinning and slot-die coating processes. Symmetric lithium cell cycling shows a three-fold increase in CCD for 50 wt% LLZO over 0 wt% LLZO, despite having similar bulk ionic and interfacial conductivities. Half cell cycling with copper, steel, and titanium electrodes shows similar CCDs, but the CE decreases from a maximum of 88% at 0 wt% LLZO to 40-60% at 50 wt% LLZO. Varying the LLZO loading shows a distinct trade-off in performance, where more LLZO results in higher CCD but significantly lower CE, even at very low LLZO loadings. Atomic force microscopy shows that CPEs have Young's and shear moduli at least one order of magnitude lower than lithium metal, well below the threshold required to mechanically prevent lithium metal from forming dendrites due to deformation. Mesoscale modelling reveals that the increase in CCD is only due to the stiff LLZO fibers forcing the lithium dendrites to plastically deform, push, and/or grow around the

fibers, resulting in lower effective dendrite growth velocity. This mechanism of high-tortuosity lithium growth through the soft PEO-LiTFSI around the LLZO is supported with time-of-flight secondary ion mass spectrometry (ToF-SIMS) imaging. Our results, even in the absence of ionic conductivity enhancements from the ceramic components, highlight important microstructural and chemomechanical aspects of CPEs and separators in general for lithium metal batteries.

Materials and Methods

Materials

Electrospinning precursor components, including lithium nitrate ($LiNO_3$), lanthanum (III) nitrate hydrate ($La(NO_3)_3 \bullet xH_2O$), zirconium (IV) oxynitrate hydrate ($ZrO(NO_3)_2 \bullet xH_2O$), and aluminum nitrate nonahydrate ($Al(NO_3)_3 \bullet 9H_2O$) were purchased from Sigma, while polyvinylpyrrolidone (PVP, average MW = 1.3 MDa) was purchased from Fisher Scientific. Polyethylene oxide (PEO, M_v = 600 kDa) was purchased from Sigma. Dimethylformamide (DMF), lithium bis(trifluoromethanesulfonyl)imide (LiTFSI), and acetic acid were purchased from Sigma. LiTFSI was stored under an Ar-atmosphere until use. Acetonitrile and isopropanol were purchased from Fisher Scientific.

Lithium foil electrodes with 250 μm thickness were purchased from MTI (USA) and freshly polished prior to cell assembly. Copper (Cu) and stainless steel 316 (SS) foils with 50 μm thickness were purchased from McMaster Carr (USA). Titanium (Ti) foil with 127 μm thickness was purchased from Trinity Brand Industries (USA). Metal electrodes were punched into 1.0 cm^2 area circles, cleaned in acetone, isopropanol, and MilliQ water, then dried under vacuum at 60 °C before transfer to the glovebox. Lithium iron phosphate (LFP) laminate cathodes were purchased from MTI (USA) and had 12 mg/cm^2 active material coated with carbon on Al foil. Cathode discs with 1.0 cm^2 areas were punched, impregnated with a small amount of PEO-LiTFSI in MeCN, and dried under vacuum at 60 °C for at least 24 hours before transfer to the glovebox.

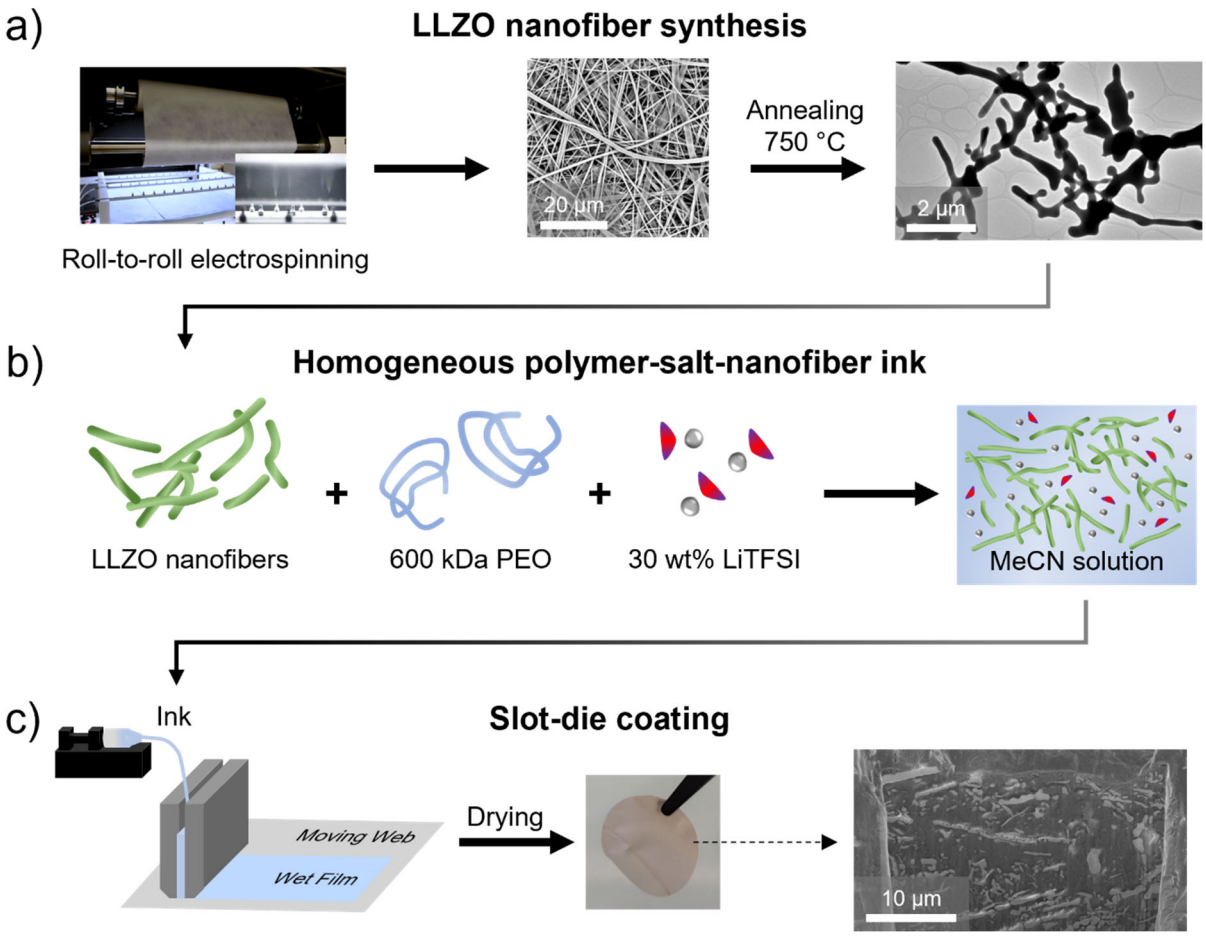

Figure 1. CPE Fabrication a) LLZO nanofibers are prepared by roll-to-roll electrospinning of precursor-loaded fibers (left and middle), followed by annealing to yield cubic LLZO with high aspect ratio (right). b) The electrolyte slurry is prepared by mixing LLZO nanofibers with PEO-LiTFSI (15:1 EO:Li mol ratio) in acetonitrile. c) Electrolyte ink is cast by slot-die coating onto a moving web, followed by drying at room temperature to yield dense CPE membranes.

Fabrication of CPEs

Composite polymer electrolytes were fabricated using two industrially scalable methods: roll-to-roll electrospinning and slot-die coating. Electrospinning generates nanofibers that can be annealed at lower temperatures (ca. 700-800 °C) to generate cubic LLZO compared to typical bulk syntheses that generate LLZO particles (ca. 1100 °C), thus saving on energy costs.[24,25] Nanofibers also present continuous percolation pathways to transport Li^+ more efficiently than typical nanoparticles.[13,26] Slot-die coating is preferable to dropcasting for membrane fabrication because it is more reproducible over large areas, can deposit multiple conformal layers, and is capable of generating membranes of <20 µm thickness, which is important for practical solid-state batteries that minimize membrane volume and weight.[27] This type of coating technology is already used industrially to coat active materials in lithium ion batteries.[28] Thus, it is of interest to understand the properties of solid-state batteries fabricated specifically with these techniques.

To generate LLZO nanofibers, a solution of PVP mixed with LLZO precursor salts was electropsun onto aluminum foil using a pilot line electrospinning unit (Inovenso, Turkey), then transferred to a quartz crucible and annealed in air at 750 °C for 2 hours at 10 °C/min. A nominal composition of $Li_{6.4}Al_{0.2}La_3Zr_2O_{12}$ was targeted, with 18% excess Li salt added to compensate for Li loss during annealing. The resulting Al-doped LLZO nanofibers have high aspect ratios with average thicknesses around 200 nm and lengths >1 μm (**Figure 1a**) and exhibit a cubic LLZO structure (**Figure S1**). The LLZO nanofibers were then transferred to an Ar-filled glovebox, annealed further at 625 °C for 30 min, and stored for later use. This temperature was chosen to remove surface carbonates[29] and reverse any proton exchange[30] in the LLZO structure from the first annealing step without using higher temperatures that could cause lithium volatilization. LLZO nanofibers coated with thin alumina layers (Al_2O_3@LLZO) were prepared with atomic layer deposition (ALD), which was carried out in a custom-built viscous flow reactor with a similar process as described previously.[31] Trimethyl aluminum (Sigma Aldrich) was used as the aluminum source and water was used as the oxygen source.

To form free-standing CPE membranes, LLZO nanofibers were mixed with PEO and LiTFSI in acetonitrile to form a homogeneous slurry over several hours (**Figure 1b**). The molar ratio of EO units to LiTFSI was constant at 15:1. The samples are denoted by the relative mass of LLZO nanofibers to the total membrane, given as wt% LLZO. For example, in most cases, the ratio of LLZO to PEO-LiTFSI was 50:50 wt:wt. The weight ratio of 50 wt% LLZO corresponds to approximately 20 volume percent LLZO in the polymer phase given densities of 5.1 g/cm^3 and 1.3 g/cm^3 for LLZO and PEO-LiTFSI, respectively. We chose to focus on this ratio for most experiments to 1) maximize the usable LLZO content and increase the likelihood of LLZO affecting the electrochemical properties while maintaining usable conductivity and 2) to mimic the higher weight loadings of polymer-infiltrated nanofiber networks.[17, 32] The total slurry concentration for slot-die coating was 18 wt% solids and 82 wt% solvent, and subsequent coating was performed at room temperature. The slurry was then cast using a slot-die coater (FOM, Denmark) onto a moving web under ambient conditions, and the film was allowed to dry for several hours before being cut into 5/8" diameter membranes and vacuum-transferred to an Ar-filled glovebox for cell assembly. The thickness of the membranes was controlled by adjusting the coating gap, solute content of coating ink, and coating speed. With this, we achieved membranes of uniform thicknesses of 80-130 μm (depending on slot-die conditions) with ≤3 μm thickness variation across a given membrane and LLZO nanofibers distributed throughout the membrane (**Figure 1c, Figures S2-S4**). PEO-LiTFSI polymer electrolytes without added LLZO fibers were prepared similarly via slot-die coating (denoted "0 wt% LLZO" samples) were similarly dense and uniform, though with up to 8 μm thickness variations across 50-60 μm thick membranes (**Figures S2 & S4**).

In general, when the electrolyte slurry is coated and allowed to dry over time, the fibers will want to settle to the bottom of the membrane due to gravity. Based on Stokes-Einstein diffusivity, the rate of settlement of the filler particles is inversely proportional to the viscosity of the solvent. Accordingly, we avoid the precipitation of fillers by adjusting viscosity of the coating inks, which can "trap" the fibers in the bulk of polymer phase during coating and after the solvent dries. When the ink viscosity was not optimized or when the inks were not mixed by high-energy

mixing or sonication, fiber clusters or bottom sedimentation were observed; even then, many fibers were still distributed in the polymer phase. Once the membrane was dried to the solid state, there was no re-distribution of the fibers, even in the melted PEO state (over the 2-14 days' timescale of cell testing). SEM and AFM measurements on the top and bottom surfaces of these composites at room temperature (**Figures S3 & S9**) show no apparent difference in microstructure, indicating there is no segregation of LLZO to the electrolyte surfaces during processing. All slot-die coated membranes show dense interior structures (**Figures S2 & S3**), indicating this roll-to-roll process produces robust, reproducible electrolytes.

Materials Characterization

Scanning electron microscopy (SEM) with energy-dispersive X-ray analysis (EDX) was performed on a Hitachi S-4700-II SEM. Focused ion beam (FIB) milling (Zeiss 1540XB FIB-SEM) was performed on some CPE surfaces prior to SEM imaging to reveal the interior and near-surface structure. Transmission electron microscopy was performed on a JEOL JEM-2100F TEM. X-ray diffraction was performed on a Bruker D8 Advance XRD. Atomic force microscopy (AFM) was performed on a Bruker Dimension Icon with peak force quantitative nanomechanical mapping (PF-QNM) module using TESPA-V2 tips (nominal 37 N/m spring constant). AFM data were processed in NanoScope Analysis software.

ToF-SIMS Imaging

Time-of-flight secondary ion mass spectrometry (ToF-SIMS) imaging was performed using a ToF-SIMS V instrument (IONTOF, Germany). Secondary ion images were acquired using a 30 keV Bi_3^+ analysis beam with a current of 0.23 pA at 200 µs cycle time focused to give a spatial resolution of approximately 2 µm. Since SIMS is a surface sensitive technique, an additional sputtering beam is required to remove surface layers to access bulk material. Here, we used 20 keV Ar_{2000}^+ with a sputter current of 10 nA from a gas cluster ion beam (GCIB) with a sputter time of 120 minutes. The instrument is operated in dual beam mode where a repeating sequence of 2D images using the Bi_3^+ analysis beam and GCIB sputtering cycles creates a 3D image data set. The Bi_3^+ analysis field of view was 200 µm × 200 µm for all samples region centered in a sputter region of 300 µm × 300 µm. Charge compensation was accomplished with a 20 eV flood gun. Cycled composite samples were prepared for ToF-SIMS by carefully removing the Li foil electrodes then GCIB milling between 7 and 120 minutes on various regions of the exposed membrane. The samples were transferred to the SIMS instrument in an Ar-filled bag and exposed to air for only a few seconds when loading into the instrument. The mass scale was calibrated with $^7Li^+$, $^6Li^+$, $^6Li^7Li^+$, and Li_2^+. The sputter depth scale was not calibrated, but an upper limit is estimated to be approximately 350 nm based on a sputter dose of 5000 ions/nm^2 and a sputtering yield volume for PMMA[33] of 0.07 nm^3/ion for argon clusters with 10 eV/atom. Since this depth is small in comparison to the field of view, the images are analyzed over a sum over all depths to give the average composition in bulk material. Data were analyzed and images prepared using SurfaceLab 7.1.130060 software.

Electrochemical Methods

Two-electrode cells were assembled in 2032 stainless steel coin cells with two 0.5 mm-thick steel spacers and a steel wave spring. All electrochemical measurements were performed with a BioLogic VSP-300 potentiostat (BioLogic, France) in temperature-controlled chambers (Maccor, USA and Espec, Japan). Cells were heated from 5 or 25 °C at 5 °C intervals up to 70 °C then back down to 60 °C, where most measurements took place; each temperature was equilibrated for at least 30 minutes before testing. This hours-long process with melted PEO ensured good wetting of the electrodes before any electrochemical measurements. Electrochemical impedance spectroscopy (EIS) was performed in the 7 MHz to 1 or 0.1 Hz frequency range, at 0.0 V vs. open circuit applied DC potential with a 10 mV sinusoidal AC amplitude, and sampling 20 points per decade. EIS data were fit using ZView software (Scribner), as in **Figure S5**. Due to inductive effects at very high frequency, only points up to 1 MHz are shown here. Galvanostatic cycling was performed under ramping conditions, starting at 10 $\mu A/cm^2$ with 10 $\mu A/cm^2$ steps, then with 20 $\mu A/cm^2$ steps above 100 $\mu A/cm^2$. Plating/charging steps were 30 minutes, followed by 30 minutes of stripping/discharging steps, or ≤30 minutes depending on the cutoff voltage (2.5 V for LFP full cells, 1.5 V for Cu, SS, and Ti half cells).

Critical current density was determined with three conditions that indicate cell shorting: a sudden (transient) voltage spike indicating a dendritic short in the cell; a deviation from expected Ohmic behavior in the cell (i.e., voltage drifting towards 0 V even without any noticeable spikes); and the appearance of electronic shunting in EIS measurements[34] taken after the galvanostatic cycle. Any single condition or combination of conditions was treated as evidence that the cell had reached its critical current density.

Results and Discussion

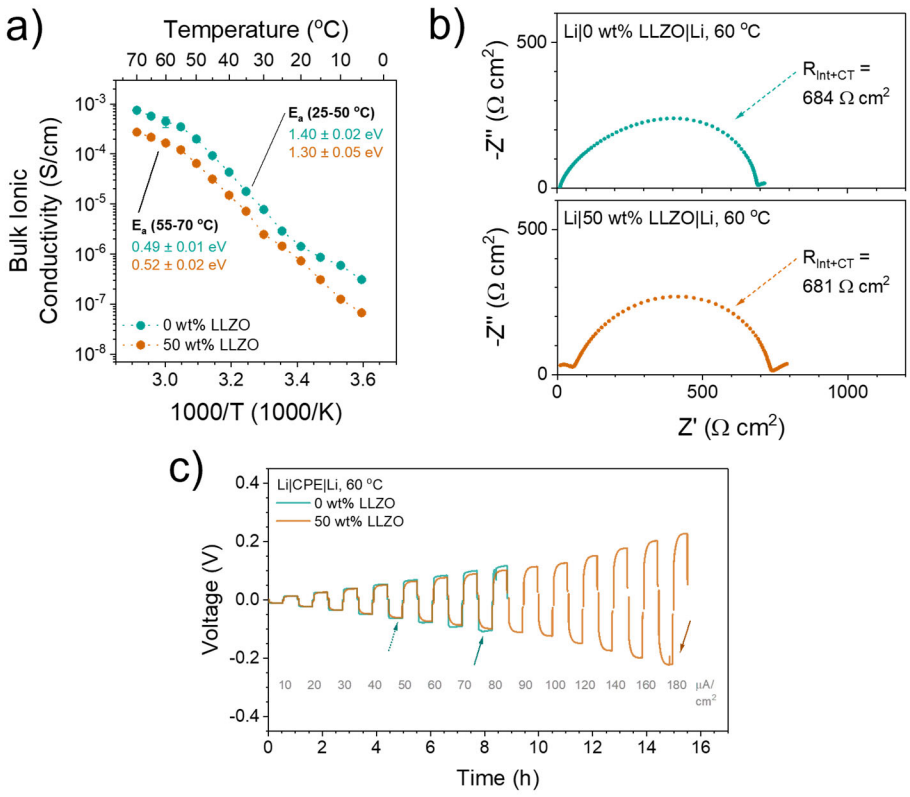

Figure 2. Lithium Symmetric Cells a) Ionic conductivity as a function of inverse temperature for 0 wt% and 50 wt% LLZO CPEs. Arrhenius activation energies for two temperature regions are shown; points and error bars represent the average and standard deviation from two different cells. b) EIS Nyquist plots of Li||Li cells with 0 wt% (top) and 50 wt% (bottom) LLZO CPEs after 4 hours at 60 °C. The combined interfacial and charge transfer resistances are noted on the graphs. c) Galvanostatic cycling of symmetric cells from 10 to 180 µA/cm^2; dashed arrows show deviations from Ohmic behavior, solid arrows show voltage spikes that definitively indicate cell shorting.

Conductivity and Lithium Symmetric Cells

In the CPE literature, there is discussion of Li^+ exchange between the ceramic LLZO phase and the polymer phase.[35,36] If this exchange is rapid, then Li^+ conductivity may proceed through the more highly conductive ceramic and not the less conductive polymer, thus increasing bulk ionic conductivity and allowing higher current densities. **Figure 2a** shows the conductivity of 0 wt% LLZO and 50 wt% LLZO composite electrolytes at various temperatures. At all temperatures, the electrolytes with 50 wt% nanofibers have lower conductivity than PEO-LiTFSI alone; this is in line with previous reports demonstrating a maximum plasticizing effect of ceramic content around 10-20 wt% before a drop in conductivity is seen.[13,14] Below 30 °C, there are slight deviations in conductivity and activation energy trends between 0 wt% and 50 wt% LLZO. These differences may be related to the Li^+ and $TFSI^-$ transport along the fiber surface or PEO plasticization, both of which can be impacted by the fiber surface's Lewis acidity or basicity.[37,38,39] Above 30 °C, all samples exhibit the same activation energies, indicating that the polymer phase

dominates ion transport at the temperatures used in our cycling. Transference number measurements (**Figure S6**) also show lower Li^+ transport with 50 wt% LLZO nanofibers than 0 wt% (t_{Li+} = 0.20 and 0.29, respectively). Thus, LLZO nanofibers in the CPEs fabricated under these conditions do not enhance conductivity, which is an important aspect relating to the performance discussed later. While our present high LLZO-loading CPEs offer relatively low bulk ionic conductivity, several methods exist in the literature for enhancing bulk Li^+ conductivity: crosslinking PEO,[40,41] plasticizing or wetting additives,[42,43, 44] varying LLZO content,[13,14] and/or modifying the LLZO interface to interact with the polymer matrix.[45,46] Many of these should be compatible with our roll-to-roll manufacturing methods. Nonetheless, our results using the most fundamental system of PEO-LiTFSI with low to high weight fractions of un-treated LLZO nanofibers should shed light on all composite electrolyte systems.

Apart from bulk resistance, interfacial resistance arising from solid electrolyte interphase (SEI) formation and charge transfer resistance play a role in cell performance. Symmetric Li||Li cells with 0 wt% and 50 wt% LLZO were assembled and analyzed with EIS over time, as shown in **Figure 2b**. The impedance related to interfacial (Int) and charge transfer (CT) resistances are apparent in two overlapping semicircles at medium frequencies (0.1-100 kHz); **Figure S5** shows the equivalent circuit and example fit of impedance for bulk and Int+CT resistances. **Figure 2b** shows that there is virtually no difference in Int and CT impedance between electrolytes without LLZO (684 Ω cm^2) and those with 50 wt% LLZO nanofibers (681 Ω cm^2) at 60 °C, indicating any differences in cycling performance are likely not due to SEI characteristics.

With identical lithium-electrolyte interfaces, bulk properties should be the main determining factor in cycling performance in these CPEs. A common parameter to benchmark performance is the critical current density (CCD), the current at which dendrites penetrate the electrolyte and short the cell. **Figure 2c** shows cycling in symmetric Li||Li cells for 0 wt% and 50 wt% LLZO electrolytes. Without LLZO nanofibers, evidence of shorting occurs at 50 μA/cm^2, followed by severe shorting at higher currents. In contrast, electrolytes with 50 wt% LLZO nanofibers can cycle up to 180 μA/cm^2 before soft-shorting occurs, as shown by transient spikes in the voltage profile that indicate lithium dendrites touching in the electrolyte before decaying. This indicates that despite lower bulk Li^+ conductivity, CPEs with LLZO nanofibers can prevent dendrites for longer periods of time. The origins of this trend are discussed below.

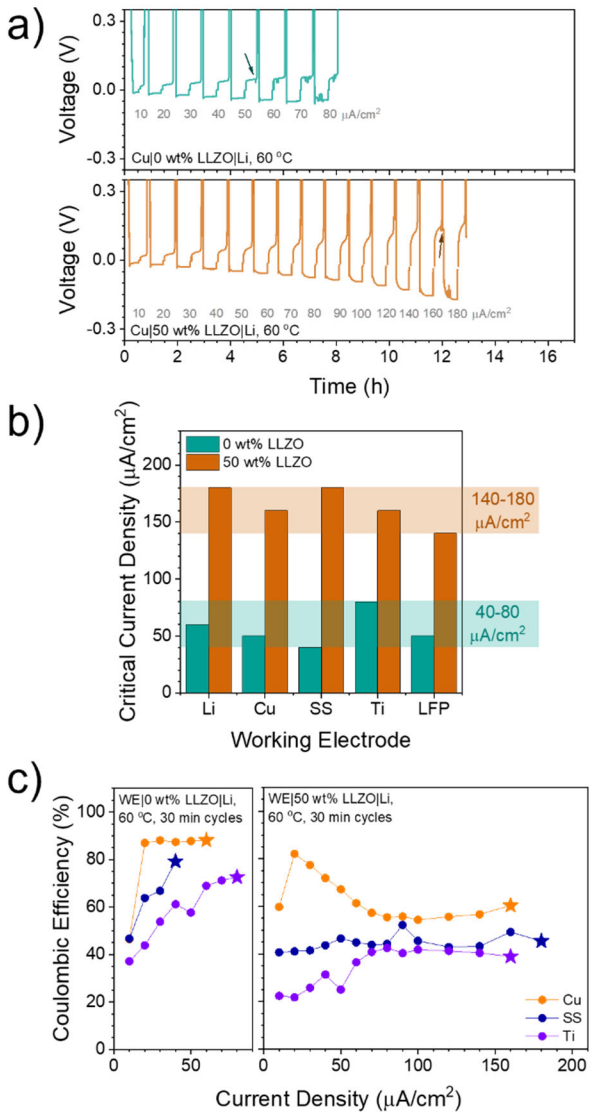

Figure 3. Half Cell Cycling, Critical Current Density, and Coulombic Efficiency a) Galvanostatic cycling of Cu||Li half cells with 0 wt% and 50 wt% LLZO CPEs. b) Critical current densities determined from galvanostatic cycling of symmetric, half, and full cells with 0 wt% and 50 wt% LLZO CPEs. c) Coulombic efficiencies calculated from galvanostatic cycling of half cells. Stars indicate CEs from the cycle in which each cell shorted.

Critical Current Density and Coulombic Efficiency

To determine if different electrode surfaces would influence critical current density apart from the bulk electrolyte properties, we performed cycling in numerous half cell configurations with copper, stainless steel, and titanium electrodes (**Figures 3a and S7**). As seen in **Figure 3a**, with copper electrodes, 0 wt% LLZO still shorts around 50 μA/cm^2 while 50 wt% LLZO persists until 160 μA/cm^2. However, the amount of lithium able to stripped in discharge steps is significantly higher in the case of 0 wt% LLZO. This indicates that LLZO plays a role in Coulombic efficiency.

Figure 3b plots the critical current density for symmetric, full, and half cells with these electrolytes. Despite differences in lithium plating that might arise from different surface chemistries, all cells have the same range of CCDs for 0 wt% and 50 wt% LLZO. Thus, the only controlling factor is the presence LLZO nanofibers, which increases the CCD from the 40-80 $\mu A/cm^2$ range to 140-180 $\mu A/cm^2$ range under these cycling conditions. It is important to note that while CCD and CE can be increased with applied pressure that maintains electrode-electrolyte contact in solid-state batteries, the cells here are under minimal pressure (an estimated ≤30 kPa from the coin cell and spring assembly),[47] which is in line with the industrial requirement of <1 MPa stack pressure.[2] Increasing transference number and conductivity are known to increase CCD,[48,49] but since our 50 wt% LLZO composites show lower overall Li^+ transference numbers and conductivity compared to 0 wt% LLZO (**Figure S6**), we do not believe enhanced ion transport is responsible for the higher current densities seen in our CPE cells.

A more thorough comparison of the Coulombic efficiency (charge stripped divided by charge plated) for all half cell samples is shown **Figure 3c** versus current density, which is also related to cell life given the cycling protocol described in the Methods section. Two trends are apparent. First, CE is more dependent on electrode material for a given CPE, with CE following the order Cu > SS > Ti. This may be related to differences in surface oxide density, lithiophilicity, surface roughness, or other factors beyond the scope of the present study.[50] Second and most importantly, electrolytes without LLZO nanofibers can reach 73-88% CE before shorting, while 50 wt% LLZO-containing samples level out to values around 40-60%. This presents a curious case where an enhancement in critical current density comes at the cost of Coulombic efficiency. This only holds if the plated Li metal penetrated the electrolyte (i.e., in the form of dendrites affected by nanofibers in the bulk) and is discussed in more detail below.

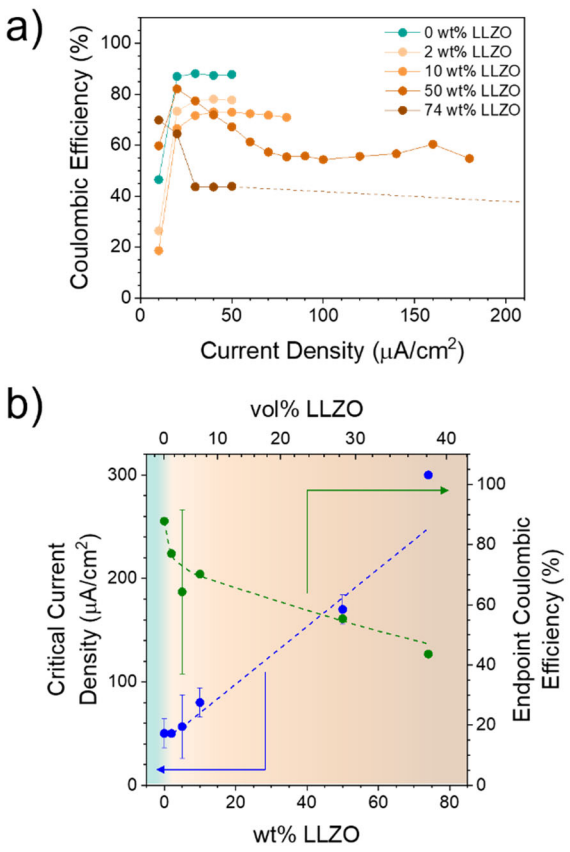

Figure 4. Nanofiber Loading Effect on Coulombic Efficiency a) Coulombic efficiencies versus current density calculated from galvanostatic cycling of Cu||Li half cells with various LLZO nanofiber loadings following the protocol in **Figure 3a**. The dashed line for 74 wt% LLZO indicates where the CE trends toward, but quantification is difficult due to the large polarization in cycling from the low conductivity of the CPE. b) Plot of critical current densities and Coulombic efficiencies prior to cell shorting as a function of LLZO nanofiber loading. Dashed lines are shown only to guide the eye. Points and error bars represent the average and standard deviation from two to three different cells. An upper estimate of 300 μA/cm^2 is given for 74 wt% LLZO, even though no shorting was seen, due to the prohibitively large polarization during cycling.

Effect of Fiber Loading on CE and CCD

Our results show that the inclusion of nanofibers increases the CCD but at the cost of charge efficiency, something critical to battery lifetime especially where there is little to no excess lithium in the cell. We varied the LLZO nanofiber loading from 0 to 74 wt% to better understand the mechanism behind this trend. We did not observe significant differences in ionic conductivity with LLZO included for the 0-10 wt% LLZO samples (**Figure S8**), again showing that conductivity differences do not play a role in the trends observed here.

Figure 4a shows the Coulombic efficiencies of Cu||Li cells with 0, 2, 10, 50, and 74 wt% LLZO composite electrolytes. After low initial CEs due to some residual SEI formation, the values level out as in **Figure 3c**. With increasing LLZO, the CEs decrease but CCDs increase, as shown

in **Figure 4b**. Surprisingly, even with 2 wt% LLZO nanofibers, which is only 0.8 vol% filler in the bulk composite, the Coulombic efficiency drops from 88% to 77%. With 5-10 wt% LLZO, generally seen as the optimum range for ionic conductivity in CPEs,[13] there is lower efficiency at ca. 70%. Higher LLZO loadings show less than 50% Coulombic efficiency, which would lead to an unacceptable amount of lithium loss early in the cell lifetime.

To our knowledge, this observation of filler inclusion lowering the Coulombic efficiency in solid composite electrolytes is the first to date, as most studies employ thick Li foil as anodes in symmetric and full cells. Zegeye *et al.* observed a 98.8% Coulombic efficiency in anode-free cells with a 10 wt% LLZO-PEO-LiTFSI coating on Cu electrodes, but their system relied on $LiPF_6$ in EC/DEC as the main liquid electrolyte.[51] For long-term battery applications, near-unity CEs are required, as any cell below 99.0% cycle-to-cycle efficiency would lose at least 63% of its lithium inventory in 100 cycles. We believe the emerging quantification of "cumulative" or "compounded" Coulombic efficiency[52, 53] will become more important in the field to address the long-term viability of anode-free cells with CPEs.

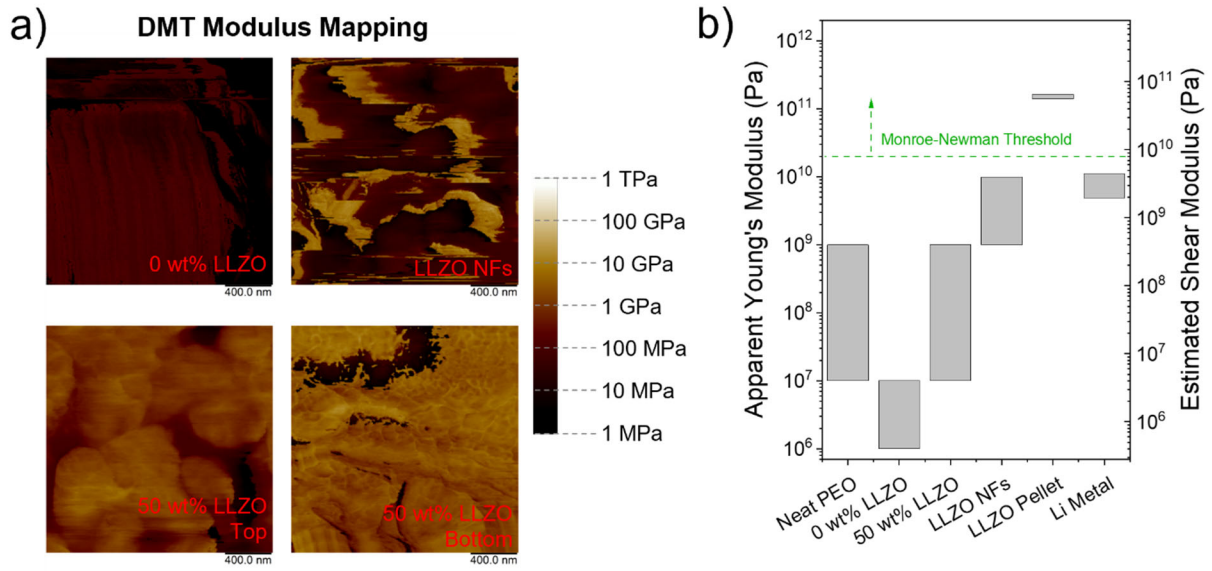

Figure 5. Microscale Mechanics of CPEs with LLZO Nanofibers a) Apparent DMT modulus from AFM imaging of a 0 wt% LLZO CPE, LLZO nanofibers, and the top and bottom surfaces of a 50 wt% LLZO CPE at room temperature. b) Comparison of Young's moduli and calculated shear moduli ranges of different materials from AFM in this work and LLZO pellets and Li metal from literature.

Macro- vs. Microscopic Bulk Effects on Dendrite Propagation

It is often postulated in the field that adding hard ceramic fillers increases the macroscopic stiffness of the CPE, with a Young's and/or shear modulus large enough to prevent lithium dendrite penetration and theorized to increase critical current density.[54] To determine if this is accurate at the microscale – the true scale that applies to dendrites that are usually less than one micron in size – we employed AFM with nanomechanical mapping. **Figure 5a** shows the DMT modulus (an

approximation of the Young's modulus) of the CPE materials; more images with height and DMT maps can be found in **Figure S9**. PEO with LiTFSI alone shows very low modulus (≤10 MPa), while the LLZO nanofibers have moduli of 1-10 GPa. When combined in a 50 wt% LLZO CPE, both the top and bottom surface of the membrane show moduli between 10 MPa and 1 GPa. This presents two important factors for dendrite formation and propagation: 1) the heterogeneity shows regions of pure polymer amid the LLZO mixture, and 2) wherever there is LLZO present, its effective modulus is lower than pure LLZO, either due to inherently lower modulus at the nanoscale or due to being covered by a thin layer of PEO-LiTFSI. These modulus ranges lower than the Young's modulus of lithium metal (5-11 GPa) have been observed previously in LLZO nanosheets and composite electrolytes with nanoindentation.[55, 56]

Figure 5b compares these numbers with those of LLZO and lithium metal reported in literature at room temperature.[57] Also shown is the shear modulus, estimated from the relationship $G = E/(2\times(1+\nu))$, where G is the shear modulus, E is the Young's modulus, and ν is the Poisson's ratio, which is around 0.25 for both LLZO and solid polymer electrolytes.[57, 58] It is clear that CPEs with up to 50 wt% LLZO nanofibers, while stronger than PEO-LiTFSI alone, do not reach the stiffness required to block lithium metal dendrite propagation into the bulk, which was determined to be double the shear modulus of lithium metal by Monroe and Newman.[54] Additionally, the softer regions of PEO-LiTFSI around and in between the fibers in the composite matrix present easy routes for penetration of lithium metal compared to LLZO. Combined with our correlation of LLZO content, CCD, and CE, we propose that there must be lithium deposition into the near-interface and/or bulk of the electrolyte through the PEO-LiTFSI phase regardless of LLZO content, which is then negatively influenced by the nanofibers.

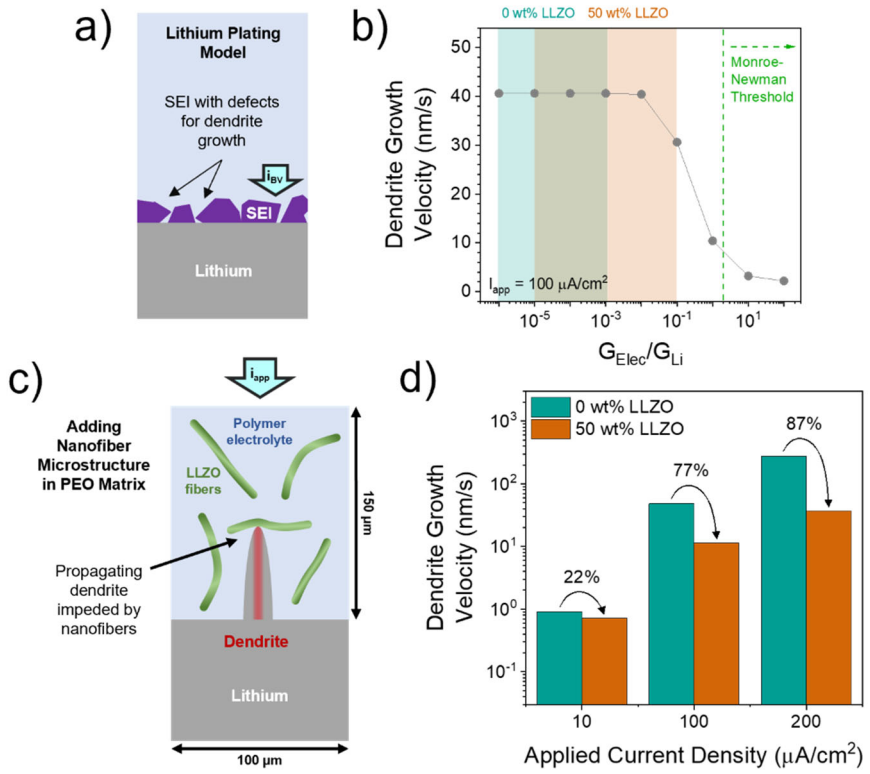

Figure 6. Modelling Dendrite Velocity a) Schematic of the model used for calculating dendrite velocity during plating on a lithium anode. Model details can be found in the SI. b) Calculated dendrite growth velocities through an imperfection in the SEI as a function of relative electrolyte shear modulus, G_{Elec}/G_{Li}. The expected G_{Elec}/G_{Li} values for the CPEs used here at 25-60 °C and the theoretical minimum needed to prevent dendrite growth from Monroe and Newman[54] are marked. c) Schematic of the model similar to a) with specific incorporation of the nanofiber microstructures. Listed sizes are the model dimensions; nanofibers and dendrite are not to scale. d) Calculated dendrite growth velocities at various current densities without (0 wt% LLZO) and with (50 wt% LLZO) the inclusion of explicit nanofibers as in c), listed with the percent drop in relative velocity with nanofiber microstructures incorporated.

To better understand how the macroscopic and microscopic electrolyte properties influence dendrite propagation in CPEs, we used mesoscale modelling to calculate dendrite growth velocities in difference CPEs. **Figure 6a** depicts a typical lithium-electrolyte interface, where the SEI has heterogeneous surface coverage and can allow dendrites to grow through the SEI at some defect, e.g., the boundary between separate SEI components. For this study, the shear modulus of the SEI, G_{SEI}, was assumed to be equivalent to that of the solid electrolyte itself, G_{Elec}. With a given G_{SEI}, the apparent dendrite velocity – i.e., the rate of dendrite growth from the anode into the electrolyte – was determined at different values of electrolyte shear modulus. **Figure 6b** plots these simulated dendrite growth velocities against the electrolyte shear modulus normalized by that of Li metal, G_{Elec}/G_{Li}; the shear modulus of Li is taken as 4.2 GPa. The approximate G_{Elec}/G_{Li} ranges of PEO-based CPEs based on AFM measurements and other experimental and computational works[35,59,60] are marked. We can consider "weak" electrolytes as having $G_{Elec}/G_{Li} < 10^{-3}$, while "strong"

electrolytes have $G_{Elec}/G_{Li} > 10^1$. Notably, all CPEs are considered "weak" electrolytes, despite incorporating 50 wt% of hard LLZO into the composite, leading to a rapid dendrite growth velocity of more than 30 nm/s at 100 μA/cm^2. As mentioned above, all CPE electrolytes are well below the threshold proposed by Monroe and Newman, requiring an interfacial shear modulus of at least two times G_{Li} to prevent dendrite propagation.[54] This should inform future studies on how to limit dendrites by modifying the interface with components apart from the native composite electrolyte.

Since neither electrolyte modulus differences nor SEI differences explain the three-fold increase in critical current density observed for CPEs with LLZO nanofibers, we modified the model to explicitly add in the microstructure of the composite, where nanofibers with modulus higher than Li metal are present (ca. 20 vol%) in the soft PEO matrix (**Figure 6c**). The velocity of a propagating dendritic protrusion is estimated using the same computational scheme. For the polymer electrolyte (0 wt% LLZO), the dendritic protrusion can easily propagate through the soft polymer layer. However, in the case of composite electrolytes (50 wt% LLZO), a propagating dendrite can encounter the LLZO nanofiber. Due to its higher mechanical stiffness, it is impossible for the dendritic protrusion to penetrate through the LLZO fiber. In order to propagate to the counter electrode, the dendritic protrusion has to either push the LLZO fiber towards the opposite electrode or find a pathway around it, which can increase the surface area and tortuosity of the dendritic protrusion. Using the developed computational framework, LLZO fiber-induced changes in the growth velocity of the dendritic protrusions were investigated. Branching of the dendritic protrusion, while likely, is not considered here; only the nanofiber being pushed towards the counter electrode by the growing lithium is taken into account.

The dendrite velocity through PEO alone or PEO with LLZO microstructures was calculated at different current densities as shown in **Figure 6d**. The inclusion of LLZO nanofibers decreases the overall dendrite velocity at all currents, slowing growth by 22% at 10 μA/cm^2 to as much as 87% at 200 μA/cm^2. In this case, we attribute the slowing of the lithium protrusions to the plastic deformation of metallic lithium, which is only observed when the dendritic protrusion comes in contact with the stiff LLZO fibers.[61,62,54] Propagation of lithium dendrites through soft PEO does not produce enough mechanical stress to lead to plastic deformation of the metal. Also, the plastic deformation of lithium becomes more prominent at higher current densities because more lithium gets deposited at the protrusion tip at higher currents, which results in enhanced stress and subsequently more plastic deformation.

Lower Coulombic efficiency in CPEs with ceramic fillers could be caused by two primary factors. First, the lithium metal could be chemically reacting with the electrolyte, essentially losing charge through corrosion in much the same way an SEI is formed. However, **Figure 2b** shows that CPEs with and without high LLZO loading have the same chemical reactivity with Li metal, which is not influenced by LLZO. If chemical reactivity was the primary cause for efficiency loss, then one would expect the same CE values with any amount of LLZO since LLZO is known to be kinetically stable against Li metal.[63] Second, the plated lithium metal could be mechanically broken or otherwise made unavailable by the nanofiber fillers to create dead lithium deposits in the near-interface or bulk. If plated lithium forms filaments, these can easily penetrate the soft polymer phase but will be blocked or split by the stronger LLZO. Along similar lines, LLZO

particles may move into and break a lithium filament already formed in the polymer phase, the so-called "razor effect" proposed by Mezzomo *et al.*[64] In either case, (dead) lithium metal deposits should be contained around the LLZO nanofibers.

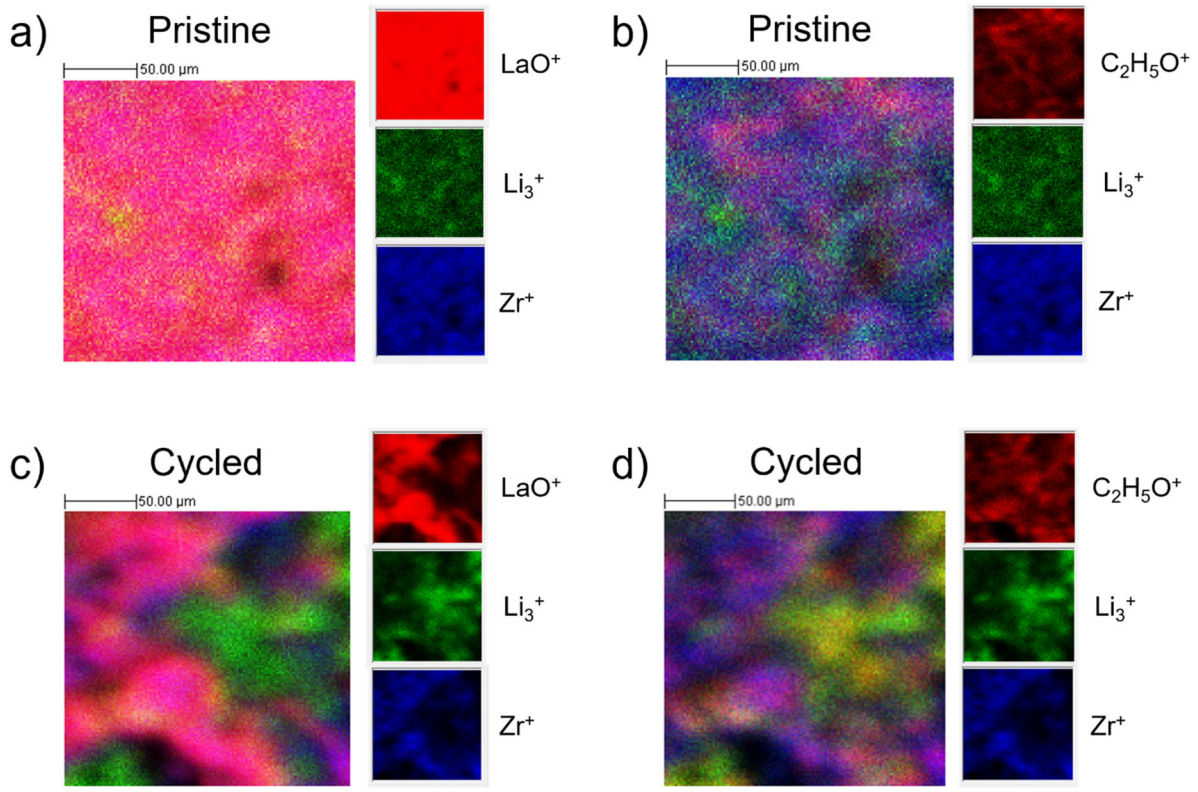

Figure 7. ToF-SIMS Imaging of Dendrites in CPEs Elemental maps of a-b) an uncycled 50 wt% LLZO CPE and c-d) cycled and shorted 50 wt% LLZO CPE. Images in a) and c) relate to the overlap of Li_3^+ and LLZO components alone; images in b) and d) relate to all polymer, Li_3^+, and LLZO components. Images are 2D reconstructions of the 3D sputtered data set by summing over depth for each pixel; see **Figure S12** for 3D reconstructions.

Table 1. List of masses and mass accuracies used in ToF-SIMS analysis and image generation.

Ion	m/z	Deviation (ppm)
Li_3^+	21.0515	191.4
$C_2H_5O^+$	45.0516	402.6
Zr^+	89.9357	350.3
LaO^+	154.9744	475.9

To confirm this hypothesis, we purposefully generated dendrite-rich Li||Li cells with 50 wt% LLZO CPEs with high-current cycling (**Figure S10**) and analyzed the CPE membrane with ToF-SIMS imaging. **Figure 7** shows elemental maps of pristine and cycled membranes with $C_2H_5O^+$ representing the PEO-based polymer phase, Zr^+ and LaO^+ representing the LLZO nanofibers, and Li_3^+ representing dense lithium clusters; the mass accuracies for these ions are

given in **Table 1**. These 2D maps are reconstructions of the 3D image data by summing over depth for each pixel and consequently are representative of material beyond the topmost surface. Since Li^+ ions are distributed everywhere in the polymer and ceramic phases, the Li_1^+ signal is not a good measure for dendrite detection. Conversely, Li_3^+ clusters are more representative of metallic lithium or reacted products involving high concentrations of lithium (like SEI), as the Li atoms are packed more closely and will be ablated as a small cluster more so than spatially separated Li^+ ions.[65] Note that the sampling region for an individual ion impact is limited to only a few nanometers, so that the probability of forming a Li_3^+ cluster is low if Li is evenly dilute. Comparison of Li_1^+ and Li_3^+ images are given in **Figure S11**, showing uniform Li_1^+ distribution from the bulk electrolyte does not yield the Li_3^+ structures seen in the cycled CPE and indicating that Li_3^+ clusters only arise from structures formed during high current cycling. The overlap of Li^+, Li_3^+, and LaO^+ and ZrO^+ signals in the pristine sample also show that the higher intensity Li_3^+ structures in the cycled case are not from LLZO.

Uncycled samples show overlapping signals from PEO and LLZO components, indicating a homogeneous mixture of polymer and ceramic phases. The Li_3^+ signal here is low (5-6 times weaker than the cycled sample) since no Li metal is present but is shown in **Figures 7a & 7b** and **Figure S11** for comparison. In contrast, the cycled composite shows distinct heterogeneity. As apparent in **Figure 7c**, the LLZO signal is entirely separate from strong Li_3^+ features, and only the PEO signal overlaps significantly with Li_3^+ as shown in **Figure 7d**. This suggests that Li_3^+ structures may preferentially grow through the polymer phase and around the fibers. Judging by the segregation of the fibers from **Figure 7a** to **Figure 7c**, the LLZO nanofibers either moved away from or were directly pushed around as a result of the Li-dense structures during cycling. **Figure S12** shows this segregation of Li_3^+, polymer, and LLZO in three dimensions. This is an interesting phenomenon that may have implications for ion transport in the electrolyte long-term, such as constricting the polymer pathways for Li^+ transport or shifting any LLZO microstructures in the as-synthesized membranes that would be desired for fast ion conduction. Additionally, it is clear in the cycled images that the Li_3^+ structures branch or multiple structures form over the course of cycling, since areas as large as 1000 μm^2 can be seen in the cross-section in different regions. More ToF-SIMS images on separate regions (**Figure S10**) show similar trends across the whole membrane area.

Effect of Filler Characteristics

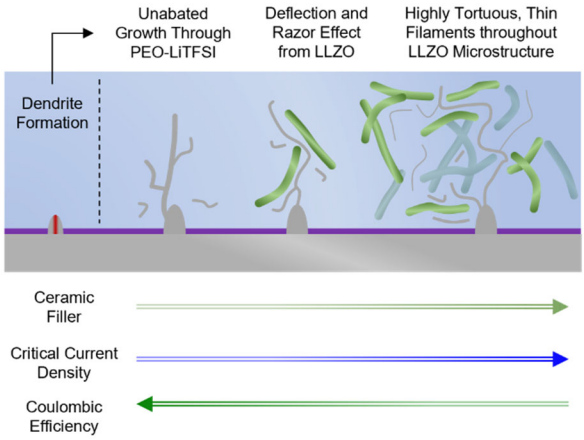

Figure 8. Role of Filler in CPE Performance Schematic of the proposed dendrite growth and propagation mechanism with increasing LLZO nanofiber content. Increased filler leads to longer pathways for dendrites to reach the positive electrode and boosts critical current density, but this leads to more branched lithium deposits and thus lower Coulombic efficiency.

In a realistic three-dimensional PEO-LLZO composite electrolyte, branching of dendritic protrusions is also possible when it encounters a LLZO fiber, which can effectively cause slowing of dendrite growth due to the inherent tortuosity of the microstructure. A dendrite growing through the polymer phase is blocked by the hard LLZO fiber, and so must grow around it, taking a longer path in 3D space to the counter electrode than the linear path afforded by PEO-LiTFSI alone (**Figure 8**). Separator tortuosity is known to inhibit dendrite formation and increase critical current density in liquid electrolytes[66] and non-Li^+-conducting ceramic-polymer composites,[67] and we partially attribute the same phenomenon to the enhanced cycling seen in our CPEs. This mechanism also explains the trend of CE with increasing nanofiber content. Tortuosity resulting in dendrite branching would create thinner lithium deposits that are more prone to breaking into dead lithium, explaining the lower CE when fibers are added. While we do not currently have the computational capabilities to address this, it presents an important aspect of CPE design where microstructure, in addition to conductivity and mechanical strength, should be a primary focus for creating high efficiency solid-state lithium metal batteries. Gao *et al*. recently reported design rules for separator porosity, spacing, and thickness to limit dendrite propagation and dead lithium formation;[68] we believe these can be applied to Li^+-conducting nanofiber structures in CPEs as well. Our results also show that it is important to prevent dendrites from forming in the first place – bulk microstructure may slow dendrite growth, but only a strong and homogeneous electrode-electrolyte interface can ensure safe lithium metal cycling in the long term.

Changing the chemistry of the nanofiller will change the Li^+ conductivity and reactivity toward lithium metal, both of which can influence dendrite propagation and Coulombic efficiency. To retain the same fiber morphology and mechanical properties but vary surface chemistry and block any possible Li^+ transport through the LLZO nanofibers, we fabricated nanofibers with a 7 nm Al_2O_3 conformal coating and made 50 wt% Al_2O_3@LLZO composite electrolytes. These composites have similar bulk conductivity and interface impedance compared to those with unmodified LLZO but have lower Li^+ transference numbers due to the blocking surface layer, as shown in **Figure S13**. The critical current density of Li||Li and Cu||Li cells remains around 180

μA/cm^2, the same range as neat 50 wt% LLZO CPEs, regardless of these chemical and Li^+ conductivity differences. The Coulombic efficiency of a Cu||Li half cell with 50 wt% Al_2O_3@LLZO nanofibers is in the range of 60-73%, which is higher than the 60% endpoint CE with unmodified fibers but lower than 88% CE with 0 wt% LLZO. The similar increase in current density agrees with our dendrite propagation mechanism supported by computation and ToF-SIMS imaging. The differences in CE at higher current densities may point to differences in lithium filament propagation with different surface chemistries. Interestingly, if the lithium metal was reacting chemically with the fibers, it is expected that Al_2O_3 coatings should lower the CE, since Li metal can reduce Al_2O_3[69] but should be kinetically stable against LLZO. The experimental observation of the opposite may point to differences in plastic deformation when contacting the modified nanofibers, leading to lower surface area morphologies that are easier to strip than with bare LLZO composites. More work into the effect of filler chemistry is needed to investigate these more subtle differences in CE, but we believe the mechanism of microstructure being the main determinant of CCD when dendrites are formed should hold for any filler.

Another important aspect of CPE design in general is the distribution of the ceramic filler in the polymer matrix. The volume percent as well as spatial ordering of nanofibers can influence both bulk ionic conductivity and interfacial lithium deposition behavior, both of which would control Coulombic efficiency and overall cell lifetime. With respect to ionic conductivity, LLZO distribution in the bulk electrolyte is important as far as establishing a percolation network[70] between fillers to establish long-range Li^+ transport. If the nanofibers are separated in space, as well as by polymer layers that have high barriers to Li^+ exchange between ceramic and polymer phases, then the polymer phase will dominate ionic transport and have low conductivity.[20] This is seemingly the case for our composites, with a random distribution of fibers throughout the bulk surrounded by PEO-LiTFSI (**Figures S2-S4**). Low Li^+ conductivity results in concentration gradients that lead to dendrite formation, which will lead to dead lithium (lower cycle-to-cycle efficiency) and short the cell (shorter lifetimes).

For lithium deposition morphology independent of conductivity, ceramic filler distribution at the interface matters more than in the bulk. One can imagine "asymmetric" composite designs, where a high volume fraction of ceramic nanofibers are segregated at the anode interface. This is postulated to increase the mechanical strength near the surface,[10, 51] preventing dendrites by physically blocking lithium penetration. Our results suggest that, unless the nanofibers significantly contribute to ionic conductivity and suppress dendrites by preventing concentration gradients, the mechanically heterogeneous microstructure of the composite would lead to a highly tortuous pathway that would lead to dendrite fragmentation rather than direct mechanical suppression of dendrites. Free nanofibers that experience uncontrolled Brownian motion in the electrolyte are also responsible for the razor effect,[64] so permanently holding the nanofibers in place via covalent linkages to the particle surface and crosslinking the polymer matrix around this scaffold[32, 45] could help limit lithium loss.

Purposefully aligning nanofibers within the composite and at the interface is another method proposed to control lithium growth. Plating within nanoscale, electrode-perpendicular channels was shown with phase field models to prevent uncontrolled lithium dendrite growth,[71, 72] something also shown experimentally with silver electrodeposition in confined polymer electrolyte channels.[73] While conceptually interesting, this approach limits the volumetric density of the lithium anode and may present problems during stripping for anode-free batteries. Lithium deposition with separators having pores parallel to the electrode surface, analogous to aligning

nanofibers in planes against the electrode, is predicted to control dendrite formation and even revive dead lithium depending on the separator dimensions.[68] Recent computational modelling predicted that ceramic ordering at the lithium metal interface in composites can lead to heterogeneous lithium plating due to uneven Li^+ transport, and that a polymer interlayer at the interface – as fabricated from our composite production process – is one solution to this issue for even lithium plating.[74]

Keeping in mind these nuances of inherently heterogeneous composite polymer electrolytes, any significant benefits from ionic conductivity and dictated lithium deposition should lead to more homogeneous, dense lithium deposits that should be easily stripped on discharge. This would lead to increased Coulombic efficiency over many cycles, limiting lithium inventory loss and extending battery lifetime. While these and similar electrolyte fabrication schemes may be used to raise the efficiency from 80% to 90% or even 99%, the true challenge is the "final hurdle" from 99% to >99.95%, the threshold for 60% capacity retention after 1000 cycles.

Conclusions

This work explores how the presence of LLZO filler in a composite polymer electrolyte influences the growth of lithium dendrites and ultimately reduces Coulombic efficiency while raising critical current density. We used roll-to-roll electrospinning and slot-die coating techniques to manufacture composite polymer electrolytes with LLZO nanofiber ceramic additives in a PEO-LiTFSI polymer matrix. While CPEs with and without LLZO show identical cell resistances and similar bulk ionic conductivities, electrolytes with 50 wt% LLZO have three times higher critical current densities than 0 wt% LLZO (140-180 $\mu A/cm^2$ vs. 40-80 $\mu A/cm^2$), regardless of the electrodes used. However, this comes at the cost of Coulombic efficiency, as demonstrated in copper half cells where the CE drops from 88% at 0 wt% LLZO to below 60% at higher loadings. Nanomechanical mapping of CPEs and mesoscale modelling of dendrite growth velocity show that the inclusion of LLZO nanofibers does not increase the micro- or macroscopic stiffness of the electrolyte to a high enough value to prevent dendrite propagation and cell shorting. Only the inherent microstructure of the stiff LLZO fibers can explain the observed increase in CCD, where the LLZO fibers cause the growing lithium filaments to slow down by plastically deforming and growing around and/or pushing the fibers. ToF-SIMS imaging corroborates this interpretation, with lithium-rich structures being found only in the polymer phase and apart from segregated LLZO fibers after cycling at high currents. Although our work has not demonstrated Li^+ conduction through LLZO fibers due to disconnection between fibers or low inherent ionic conductivity, our result does not discredit the application of Li^+-conducting ceramic fillers that demonstrably improve CPE performance. Instead, we suggest that dendrite growth will be affected by fillers in CPEs, and this influence is related to the filler's mechanical properties and shape in addition to chemistry and ionic conductivity. This mechanism should be taken into account when studying any composite electrolyte system, and making assumptions about the efficiency of the electrolyte with lithium symmetric cells and full cells with excess lithium anodes should be discouraged. We will apply the design rules learned here to more complex, better-performing

LLZO-in-polymer structures developed by others to have totally integrated design for practical, low-resistance, and efficient CPE applications.

Acknowledgements

This work was funded by the U.S. Department of Energy, Office of Energy Efficiency and Renewable Energy Vehicle Technologies Program with support from Simon T. Thompson and Tien Duong. Research was carried out at Argonne National Laboratory which is supported by the U.S. Department of Energy, Office of Science, Office of Basic Energy Sciences, under contract no. DE-AC02-06CH1135. Electrospinning and coating equipment were procured with funding support from the DOE-AMO Roll-to-Roll Advanced Materials Manufacturing DOE Laboratory Collaboration program. Use of the Center for Nanoscale Materials, an Office of Science user facility, was supported by the U. S. Department of Energy, Office of Science, Office of Basic Energy Sciences, under Contract No. DE-AC02-06CH11357. Use of the Materials Engineering Research Facility (MERF) at Argonne National Laboratory was supported by the U.S. Department of Energy. TZ was supported by the University of Illinois Chicago and Argonne National Laboratory work order number 0J-60008-0031A. The ToF-SIMS measurements were supported by the Energy and Environment programme of the National Measurement System of the UK Department of Science, Innovation and Technology. We thank Dr. Xinwei Zhou and Dr. Yuzi Liu for assistance with TEM analysis and Dr. Anil Mane and Dr. Jeffery Elam for assistance with ALD.

Supporting Information. Nanofiber characterization; CPE cross-section SEM; impedance fitting; transference number measurements; half cell cycling; conductivity as a function of LLZO content; AFM mapping; ToF-SIMS mapping; Al_2O_3@LLZO composite results; computational model details

References

1. Bonnick, P.; Muldoon, J. The Quest for the Holy Grail of Solid-State Lithium Batteries. *Energy Environ. Sci.* **2022,** *15* (5), 1840-1860.

2. Albertus, P.; Anandan, V.; Ban, C.; Balsara, N.; Belharouak, I.; Buettner-Garrett, J.; Chen, Z.; Daniel, C.; Doeff, M.; Dudney, N. J.; Dunn, B.; Harris, S. J.; Herle, S.; Herbert, E.; Kalnaus, S.; Libera, J. A.; Lu, D.; Martin, S.; McCloskey, B. D.; McDowell, M. T.; Meng, Y. S.; Nanda, J.; Sakamoto, J.; Self, E. C.; Tepavcevic, S.; Wachsman, E.; Wang, C.; Westover, A. S.; Xiao, J.; Yersak, T. Challenges for and Pathways toward Li-Metal-Based All-Solid-State Batteries. *ACS Energy Lett.* **2021,** *6* (4), 1399-1404.

3. Grundish, N. S.; Goodenough, J. B.; Khani, H. Designing Composite Polymer Electrolytes for All-Solid-State Lithium Batteries. *Curr. Opin. Electrochem.* **2021,** *30*, 100828.

4. Zhang, Q.; Liu, K.; Wen, Y.; Kong, Y.; Wen, Y.; Zhang, Q.; Liu, N.; Li, J.; Ma, C.; Du, Y. Advances in Solid Lithium Ion Electrolyte Based on the Composites of Polymer and LLTO/LLZO of Rare Earth Oxides. *Eng. Rep.* **2022,** *4* (1), e12448.

5. Xia, W.; Xu, B.; Duan, H.; Guo, Y.; Kang, H.; Li, H.; Liu, H. Ionic Conductivity and Air Stability of Al-Doped Li7La3Zr2O12 Sintered in Alumina and Pt Crucibles. *ACS Appl. Mater. Interfaces* **2016,** *8* (8), 5335-5342.

6. Li, Z.; Huang, H.-M.; Zhu, J.-K.; Wu, J.-F.; Yang, H.; Wei, L.; Guo, X. Ionic Conduction in Composite Polymer Electrolytes: Case of PEO:Ga-LLZO Composites. *ACS Appl. Mater. Interfaces* **2019,** *11* (1), 784-791.

7. Shen, C.; Huang, Y.; Yang, J.; Chen, M.; Liu, Z. Unraveling the Mechanism of Ion and Electron Migration in Composite Solid-State Electrolyte using Conductive Atomic Force Microscopy. *Energy Storage Mater.* **2021,** *39*, 271-277.

8. Sharma, J.; Polizos, G.; Jafta, C. J.; Wood, D. L.; Li, J. Review—Electrospun Inorganic Solid-State Electrolyte Fibers for Battery Applications. *J. Electrochem. Soc.* **2022,** *169* (5), 050527.

9. Liu, W.; Liu, N.; Sun, J.; Hsu, P.-C.; Li, Y.; Lee, H.-W.; Cui, Y. Ionic Conductivity Enhancement of Polymer Electrolytes with Ceramic Nanowire Fillers. *Nano Lett.* **2015,** *15* (4), 2740-2745.

10. Wan, Z.; Lei, D.; Yang, W.; Liu, C.; Shi, K.; Hao, X.; Shen, L.; Lv, W.; Li, B.; Yang, Q.-H.; Kang, F.; He, Y.-B. Low Resistance–Integrated All-Solid-State Battery Achieved by Li7La3Zr2O12 Nanowire Upgrading Polyethylene Oxide (PEO) Composite Electrolyte and PEO Cathode Binder. *Adv. Funct. Mater.* **2019,** *29* (1), 1805301.

11. Gong, Y.; Fu, K.; Xu, S.; Dai, J.; Hamann, T. R.; Zhang, L.; Hitz, G. T.; Fu, Z.; Ma, Z.; McOwen, D. W.; Han, X.; Hu, L.; Wachsman, E. D. Lithium-Ion Conductive Ceramic Textile: A New Architecture for Flexible Solid-State Lithium Metal Batteries. *Mater. Today* **2018,** *21* (6), 594-601.

12. Cheng, J.; Hou, G.; Sun, Q.; Chen, Q.; Li, D.; Li, J.; Zeng, Z.; Li, K.; Yuan, Q.; Wang, J.; Ci, L. A Novel Coral-Like Garnet for high-Performance PEO-Based All Solid-State Batteries. *Sci. China Mater.* **2022,** *65* (2), 364-372.

13. Din, M. M. U.; Häusler, M.; Fischer, S. M.; Ratzenböck, K.; Chamasemani, F. F.; Hanghofer, I.; Henninge, V.; Brunner, R.; Slugovc, C.; Rettenwander, D. Role of Filler Content and Morphology in LLZO/PEO Membranes. *Front. Energy Res.* **2021,** *9*, 711610.

14. Yang, T.; Zheng, J.; Cheng, Q.; Hu, Y.-Y.; Chan, C. K. Composite Polymer Electrolytes with Li7La3Zr2O12 Garnet-Type Nanowires as Ceramic Fillers: Mechanism of Conductivity Enhancement and Role of Doping and Morphology. *ACS Appl. Mater. Interfaces* **2017,** *9* (26), 21773-21780.

15. Lu, W.; Xue, M.; Zhang, C. Modified Li7La3Zr2O12 (LLZO) and LLZO-Polymer Composites for Solid-State Lithium Batteries. *Energy Storage Mater.* **2021,** *39*, 108-129.

16. Zhao, Y.; Yan, J.; Cai, W.; Lai, Y.; Song, J.; Yu, J.; Ding, B. Elastic and Well-Aligned Ceramic LLZO Nanofiber Based Electrolytes for Solid-State Lithium Batteries. *Energy Storage Mater.* **2019,** *23*, 306-313.

17. Fu, K.; Gong, Y.; Dai, J.; Gong, A.; Han, X.; Yao, Y.; Wang, C.; Wang, Y.; Chen, Y.; Yan, C.; Li, Y.; Wachsman, E. D.; Hu, L. Flexible, Solid-State, Ion-Conducting Membrane with 3D Garnet Nanofiber Networks for Lithium Batteries. *Proc. Natl. Acad. Sci. USA* **2016,** *113* (26), 7094-7099.

18. Wu, N.; Chien, P.-H.; Qian, Y.; Li, Y.; Xu, H.; Grundish, N. S.; Xu, B.; Jin, H.; Hu, Y.-Y.; Yu, G.; Goodenough, J. B. Enhanced Surface Interactions Enable Fast Li+ Conduction in Oxide/Polymer Composite Electrolyte. *Angew. Chem. Int. Ed.* **2020,** *59* (10), 4131-4137.

19. Banerjee, A.; Wang, X.; Fang, C.; Wu, E. A.; Meng, Y. S. Interfaces and Interphases in All-Solid-State Batteries with Inorganic Solid Electrolytes. *Chem. Rev.* **2020,** *120* (14), 6878-6933.

20. Chen, L.; Li, Y.; Li, S.-P.; Fan, L.-Z.; Nan, C.-W.; Goodenough, J. B. PEO/Garnet Composite Electrolytes for Solid-State Lithium Batteries: From "Ceramic-in-Polymer" to "Polymer-in-Ceramic". *Nano Energy* **2018,** *46*, 176-184.

21. Wang, M. J.; Carmona, E.; Gupta, A.; Albertus, P.; Sakamoto, J. Enabling "Lithium-Free" Manufacturing of Pure Lithium Metal Solid-State Batteries through In Situ Plating. *Nat. Commun.* **2020,** *11* (1), 5201.

22. Huang, W.-Z.; Zhao, C.-Z.; Wu, P.; Yuan, H.; Feng, W.-E.; Liu, Z.-Y.; Lu, Y.; Sun, S.; Fu, Z.-H.; Hu, J.-K.; Yang, S.-J.; Huang, J.-Q.; Zhang, Q. Anode-Free Solid-State Lithium Batteries: A Review. *Adv. Energy Mater.* **2022,** *12* (26), 2201044.

23. Acebedo, B.; Morant-Miñana, M. C.; Gonzalo, E.; Ruiz de Larramendi, I.; Villaverde, A.; Rikarte, J.; Fallarino, L. Current Status and Future Perspective on Lithium Metal Anode Production Methods. *Adv. Energy Mater.* **2023**, *13* (13), 2203744.

24. Yang, T.; Gordon, Z. D.; Li, Y.; Chan, C. K. Nanostructured Garnet-Type Solid Electrolytes for Lithium Batteries: Electrospinning Synthesis of Li7La3Zr2O12 Nanowires and Particle Size-Dependent Phase Transformation. *J. Phys. Chem. C* **2015,** *119* (27), 14947-14953.

25. Rosenthal, T.; Weller, J. M.; Chan, C. K. Needleless Electrospinning for High Throughput Production of Li7La3Zr2O12 Solid Electrolyte Nanofibers. *Ind. Eng. Chem. Res.* **2019,** *58* (37), 17399-17405.

26. Xie, H.; Yang, C.; Fu, K.; Yao, Y.; Jiang, F.; Hitz, E.; Liu, B.; Wang, S.; Hu, L. Flexible, Scalable, and Highly Conductive Garnet-Polymer Solid Electrolyte Templated by Bacterial Cellulose. *Adv. Energy Mater.* **2018,** *8* (18), 1703474.

27. Wu, J.; Yuan, L.; Zhang, W.; Li, Z.; Xie, X.; Huang, Y. Reducing the Thickness of Solid-State Electrolyte Membranes for High-Energy Lithium Batteries. *Energy Environ. Sci.* **2021,** *14* (1), 12-36.

28. Kwade, A.; Haselrieder, W.; Leithoff, R.; Modlinger, A.; Dietrich, F.; Droeder, K. Current Status and Challenges for Automotive Battery Production Technologies. *Nat. Energy* **2018,** *3* (4), 290-300.

29. Cheng, L.; Liu, M.; Mehta, A.; Xin, H.; Lin, F.; Persson, K.; Chen, G.; Crumlin, E. J.; Doeff, M. Garnet Electrolyte Surface Degradation and Recovery. *ACS Appl. Energy Mater.* **2018,** *1* (12), 7244-7252.

30. Larraz, G.; Orera, A.; Sanjuán, M. L. Cubic Phases of Garnet-Type Li7La3Zr2O12: The Role of Hydration. *J. Mater. Chem. A* **2013,** *1* (37), 11419-11428.

31. Elam, J. W.; Groner, M. D.; George, S. M. Viscous Flow Reactor with Quartz Crystal Microbalance for Thin Film Growth by Atomic Layer Deposition. *Rev. Sci0 Instrum.* **2002,** *73* (8), 2981-2987.

32. Bao, C.; Zheng, C.; Wu, M.; Zhang, Y.; Jin, J.; Chen, H.; Wen, Z. 12 μm-Thick Sintered Garnet Ceramic Skeleton Enabling High-Energy-Density Solid-State Lithium Metal Batteries. *Adv. Energy Mater.* **2023,** *13* (13), 2204028.

33. Seah, M. P. Universal Equation for Argon Gas Cluster Sputtering Yields. *J. Phys. Chem. C* **2013,** *117* (24), 12622-12632.

34. Li, Q.; Chen, A.; Wang, D.; Pei, Z.; Zhi, C. "Soft Shorts" Hidden in Zinc Metal Anode Research. *Joule* **2022,** *6* (2), 273-279.

35. Bonilla, M. R.; García Daza, F. A.; Ranque, P.; Aguesse, F.; Carrasco, J.; Akhmatskaya, E. Unveiling Interfacial Li-Ion Dynamics in Li7La3Zr2O12/PEO(LiTFSI) Composite Polymer-Ceramic Solid Electrolytes for All-Solid-State Lithium Batteries. *ACS Appl. Mater. Interfaces* **2021,** *13* (26), 30653-30667.

36. Brogioli, D.; Langer, F.; Kun, R.; La Mantia, F. Space-Charge Effects at the Li7La3Zr2O12/Poly(ethylene oxide) Interface. *ACS Appl. Mater. Interfaces* **2019,** *11* (12), 11999-12007.

37. Croce, F.; Persi, L.; Scrosati, B.; Serraino-Fiory, F.; Plichta, E.; Hendrickson, M. A. Role of the Ceramic Fillers in Enhancing the Transport Properties of Composite Polymer Electrolytes. *Electrochim. Acta* **2001,** *46* (16), 2457-2461.

38. Jayathilaka, P. A. R. D.; Dissanayake, M. A. K. L.; Albinsson, I.; Mellander, B. E. Effect of Nano-Porous Al2O3 on Thermal, Dielectric and Transport Properties of the (PEO)9liTFSI Polymer Electrolyte System. *Electrochim. Acta* **2002,** *47* (20), 3257-3268.

39. Lim, Y.-J.; An, Y.-H.; Jo, N.-J. Polystyrene-Al2O3 Composite Solid Polymer Electrolyte for Lithium Secondary Battery. *Nanoscale Res. Lett.* **2012,** *7* (1), 19.

40. Lehmann, M. L.; Yang, G.; Nanda, J.; Saito, T. Well-designed Crosslinked Polymer Electrolyte Enables High Ionic Conductivity and Enhanced Salt Solvation. *J. Electrochem. Soc.* **2020,** *167* (7), 070539.

41. Falco, M.; Simari, C.; Ferrara, C.; Nair, J. R.; Meligrana, G.; Bella, F.; Nicotera, I.; Mustarelli, P.; Winter, M.; Gerbaldi, C. Understanding the Effect of UV-Induced Cross-Linking on the Physicochemical Properties of Highly Performing PEO/LiTFSI-Based Polymer Electrolytes. *Langmuir* **2019,** *35* (25), 8210-8219.

42. Wang, J.; Yang, J.; Shen, L.; Guo, Q.; He, H.; Yao, X. Synergistic Effects of Plasticizer and 3D Framework toward High-Performance Solid Polymer Electrolyte for Room-Temperature Solid-State Lithium Batteries. *ACS Appl. Energy Mater.* **2021,** *4* (4), 4129-4137.

43. Zhao, Y.; Tao, R.; Fujinami, T. Enhancement of Ionic Conductivity of PEO-Litfsi Electrolyte upon Incorporation of Plasticizing Lithium Borate. *Electrochim. Acta* **2006,** *51* (28), 6451-6455.

44. Liu, M.; Zhang, S.; van Eck, E. R. H.; Wang, C.; Ganapathy, S.; Wagemaker, M. Improving Li-ion Interfacial Transport in Hybrid Solid Electrolytes. *Nat. Nanotechnol.* **2022,** *17* (9), 959-967.

45. Yan, C.; Zhu, P.; Jia, H.; Du, Z.; Zhu, J.; Orenstein, R.; Cheng, H.; Wu, N.; Dirican, M.; Zhang, X. Garnet-Rich Composite Solid Electrolytes for Dendrite-Free, High-Rate, Solid-State Lithium-Metal Batteries. *Energy Storage Mater.* **2020,** *26*, 448-456.

46. Li, W.; Sun, C.; Jin, J.; Li, Y.; Chen, C.; Wen, Z. Realization of the Li+ Domain Diffusion Effect via Constructing Molecular Brushes on the LLZTO Surface and Its Application in All-Solid-State Lithium Batteries. *J. Mater. Chem. A* **2019,** *7* (48), 27304-27312.

47. Tanim, T. R.; Dufek, E. J.; Evans, M.; Dickerson, C.; Jansen, A. N.; Polzin, B. J.; Dunlop, A. R.; Trask, S. E.; Jackman, R.; Bloom, I.; Yang, Z.; Lee, E. Extreme Fast Charge Challenges for Lithium-Ion Battery: Variability and Positive Electrode Issues. *J. Electrochem. Soc.* **2019,** *166* (10), A1926.

48. Lu, Y.; Tikekar, M.; Mohanty, R.; Hendrickson, K.; Ma, L.; Archer, L. A. Stable Cycling of Lithium Metal Batteries Using High Transference Number Electrolytes. *Adv. Energy Mater.* **2015,** *5* (9), 1402073.

49. Chen, L.; Li, W.; Fan, L.-Z.; Nan, C.-W.; Zhang, Q. Intercalated Electrolyte with High Transference Number for Dendrite-Free Solid-State Lithium Batteries. *Adv. Funct. Mater.* **2019,** *29* (28), 1901047.

50. Park, S.; Jin, H.-J.; Yun, Y. S. Advances in the Design of 3D-Structured Electrode Materials for Lithium-Metal Anodes. *Adv. Mater.* **2020,** *32* (51), 2002193.

51. Zegeye, T. A.; Su, W.-N.; Fenta, F. W.; Zeleke, T. S.; Jiang, S.-K.; Hwang, B. J. Ultrathin Li6.75La3Zr1.75Ta0.25O12-Based Composite Solid Electrolytes Laminated on Anode and Cathode Surfaces for Anode-free Lithium Metal Batteries. *ACS Appl. Energy Mater.* **2020,** *3* (12), 11713-11723.

52. Schulze, M. C.; Neale, N. R. Half-Cell Cumulative Efficiency Forecasts Full-Cell Capacity Retention in Lithium-Ion Batteries. *ACS Energy Lett.* **2021,** *6* (3), 1082-1086.

53. Oyakhire, S. T.; Zhang, W.; Yu, Z.; Holmes, S. E.; Sayavong, P.; Kim, S. C.; Boyle, D. T.; Kim, M. S.; Zhang, Z.; Cui, Y.; Bent, S. F. Correlating the Formation Protocols of Solid Electrolyte Interphases with Practical Performance Metrics in Lithium Metal Batteries. *ACS Energy Lett.* **2023,** *8* (1), 869-877.

54. Monroe, C.; Newman, J. The Impact of Elastic Deformation on Deposition Kinetics at Lithium/Polymer Interfaces. *J. Electrochem. Soc.* **2005,** *152* (2), A396.

55. Guo, S.; Kou, W.; Wu, W.; Lv, R.; Yang, Z.; Wang, J. Thin Laminar Inorganic Solid Electrolyte with High Ionic Conductance towards High-Performance All-Solid-State Lithium Battery. *Chem. Eng. J.* **2022,** *427*, 131948.

56. Guo, Z.; Ye, C.; Zhao, T.; Wu, W.; Kou, W.; Zhang, Y.; Dong, W.; Li, W.; Wang, J. Thin Lamellar Li7La3Zr2O12 Solid Electrolyte with G-C3N4 as Grain Boundary Modifier for High-Performance All-Solid-State Lithium Battery. *J. Power Sources* **2023,** *562*, 232784.

57. Yu, S.; Schmidt, R. D.; Garcia-Mendez, R.; Herbert, E.; Dudney, N. J.; Wolfenstine, J. B.; Sakamoto, J.; Siegel, D. J. Elastic Properties of the Solid Electrolyte Li7La3Zr2O12 (LLZO). *Chem. Mater.* **2016,** *28* (1), 197-206.

58. Grazioli, D.; Verners, O.; Zadin, V.; Brandell, D.; Simone, A. Electrochemical-Mechanical Modeling of Solid Polymer Electrolytes: Impact of Mechanical Stresses on Li-ion Battery Performance. *Electrochim. Acta* **2019,** *296*, 1122-1141.

59. Kim, H.-K.; Barai, P.; Chavan, K.; Srinivasan, V. Transport and Mechanical Behavior in PEO-LLZO Composite Electrolytes. *J Solid State Electrochem.* **2022,** *26* (9), 2059-2075.

60. Lee, J.; Howell, T.; Rottmayer, M.; Boeckl, J.; Huang, H. Free-Standing PEO/LiTFSI/LAGP Composite Electrolyte Membranes for Applications to Flexible Solid-State Lithium-Based Batteries. *J. Electrochem. Soc.* **2019,** *166* (2), A416.

61. Barai, P.; Ngo, A. T.; Narayanan, B.; Higa, K.; Curtiss, L. A.; Srinivasan, V. The Role of Local Inhomogeneities on Dendrite Growth in LLZO-Based Solid Electrolytes. *J. Electrochem. Soc.* **2020,** *167* (10), 100537.

62. Barai, P.; Higa, K.; Srinivasan, V. Effect of Initial State of Lithium on the Propensity for Dendrite Formation: A Theoretical Study. *J. Electrochem. Soc.* **2016,** *164* (2), A180.

63. Connell, J. G.; Fuchs, T.; Hartmann, H.; Krauskopf, T.; Zhu, Y.; Sann, J.; Garcia-Mendez, R.; Sakamoto, J.; Tepavcevic, S.; Janek, J. Kinetic versus Thermodynamic Stability of LLZO in Contact with Lithium Metal. *Chem. Mater.* **2020,** *32* (23), 10207-10215.

64. Mezzomo, L.; Lorenzi, R.; Mauri, M.; Simonutti, R.; D'Arienzo, M.; Wi, T.-U.; Ko, S.; Lee, H.-W.; Poggini, L.; Caneschi, A.; Mustarelli, P.; Ruffo, R. Unveiling the Role of PEO-Capped TiO2 Nanofiller in Stabilizing the Anode Interface in Lithium Metal Batteries. *Nano Lett.* **2022,** *22* (21), 8509-8518.

65. Li, W.; Kim, U.-H.; Dolocan, A.; Sun, Y.-K.; Manthiram, A. Formation and Inhibition of Metallic Lithium Microstructures in Lithium Batteries Driven by Chemical Crossover. *ACS Nano* **2017,** *11* (6), 5853-5863.

66. Rafiz, K.; Murali, D. R. L.; Lin, J. Y. S., Suppressing Lithium Dendrite Growth on Lithium-Ion/Metal Batteries by a Tortuously Porous γ-Alumina Separator. *Electrochim. Acta* **2022,** *421*, 140478.

67. Lin, D.; Yuen, P. Y.; Liu, Y.; Liu, W.; Liu, N.; Dauskardt, R. H.; Cui, Y. A Silica-Aerogel-Reinforced Composite Polymer Electrolyte with High Ionic Conductivity and High Modulus. *Adv. Mater.* **2018,** *30* (32), 1802661.

68. Gao, L. T.; Huang, P.; Guo, Z.-S. Elucidating the Role of Rational Separator Microstructures in Guiding Dendrite Growth and Reviving Dead Li. *ACS Appl. Mater. Interfaces* **2022,** *14* (37), 41957-41968.

69. Chen, L.; G. Connell, J.; Nie, A.; Huang, Z.; R. Zavadil, K.; C. Klavetter, K.; Yuan, Y.; Sharifi-Asl, S.; Shahbazian-Yassar, R.; A. Libera, J.; U. Mane, A.; W. Elam, J. Lithium Metal Protected by Atomic Layer Deposition Metal Oxide for High Performance Anodes. *J. Mater. Chem. A* **2017,** *5* (24), 12297-12309.

70. Tang, B.; Zhao, Y.; Wang, Z.; Chen, S.; Wu, Y.; Tseng, Y.; Li, L.; Guo, Y.; Zhou, Z.; Bo, S.-H. Ultrathin Salt-Free Polymer-in-Ceramic Electrolyte for Solid-State Sodium Batteries. *eScience* **2021,** *1* (2), 194-202.

71. Ren, Y.; Zhou, Y.; Cao, Y. Inhibit of Lithium Dendrite Growth in Solid Composite Electrolyte by Phase-Field Modeling. *J. Phys. Chem. C* **2020,** *124* (23), 12195-12204.

72. Li, Y.; Cao, D.; Arnold, W.; Ren, Y.; Liu, C.; Jasinski, J. B.; Druffel, T.; Cao, Y.; Zhu, H.; Wang, H. Regulated Lithium Ionic Flux through Well-Aligned Channels for Lithium Dendrite Inhibition in Solid-State Batteries. *Energy Storage Mater.* **2020,** *31*, 344-351.

73. Sharon, D.; Bennington, P.; Patel, S. N.; Nealey, P. F. Stabilizing Dendritic Electrodeposition by Limiting Spatial Dimensions in Nanostructured Electrolytes. *ACS Energy Lett.* **2020,** *5* (9), 2889-2896.

74. Barai, P.; Fuchs, T.; Trevisanello, E.; Kim, H. K.; Richter, F. H.; Janek, J.; Srinivasan, V. Reaction Current Heterogeneity at the Interface between a Lithium Electrode and Polymer/Ceramic Composite Electrolytes. *ACS Appl. Energy Mater.* **2023,** *6* (4), 2160-2177.

Table of Contents Graphic

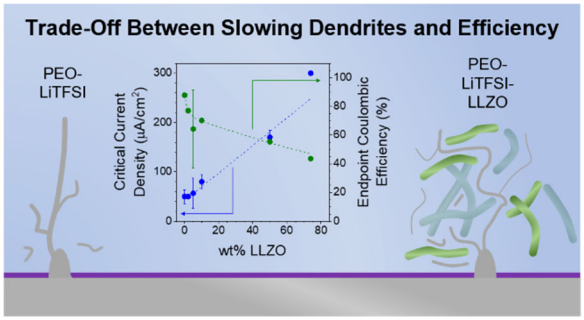

Keywords: lithium metal battery; composite; polymer; solid electrolyte; critical current; Coulombic efficiency; dendrite